Experimental investigation and model validation of the CaO/Ca(OH)$_2$ fluidized bed reactors for thermochemical energy storage applications

Yolanda A. Criado[a],*, Arthur Huille[b], Sylvie Rougé[b], J. Carlos Abanades[a]

[a]CSIC-INCAR, C/ Francisco Pintado Fe, 26, 33011, Oviedo. Spain.

[b]CEA-LITEN-LETh, 17 rue de Martyrs, F-38054 Grenoble Cedex 9, France

* Corresponding Author: Tel: +34 985119090; Fax: +34 985297662; e-mail: yolanda.ac@incar.csic.es

Abstract

The CaO/Ca(OH)$_2$ hydration/dehydration chemical loop has long been recognized as a potential candidate for application in energy storage systems for concentrated solar plants. However, the technology still remains at a conceptual level because little information has been published on the performance of the key reactors in the system. In this work, we experimentally investigate the hydration and dehydration reactors in a 5.5 kW batch fluidized bed reactor, in conditions relevant to larger systems (superficial gas velocities of up to 1 m/s, temperatures of up to 500ºC for dehydration, inlet H$_2$O$_{(v)}$ partial pressures between 0 and 0.8 etc.). Furthermore, to assist in the interpretation of the experimental results, a standard 1D bubbling reactor model has been formulated and fitted to the experimental results by including kinetic information at particle level independently measured in a thermogravimetric apparatus. The results indicate that the hydration reaction is mainly controlled by the slow kinetics of the CaO material tested while significant emulsion-bubble mass-transfer resistances were identified during dehydration due to the much faster dehydration kinetics.

1. Introduction

The energy efficiency and flexibility of renewable energies are key issues that need to be tackled to reduce their cost and facilitate their widespread deployment in order to combat climate change [1, 2]. Current concentrated solar plants (CSP) are inherently intermittent in their power supply unless they use a thermal energy storage (TES) unit [3-6]. These units not only allow the hours of plant operation to be extended, but also make the plant more versatile so that supply can be coupled to demand and the power output can be kept steady during transition periods of lower solar input [4].

TES systems based on the storage of sensible and latent heat are the standard commercial benchmarks despite their limited efficiency because of their robustness and relative simplicity [7]. Recent research has been focused on the use of thermochemical energy storage (TCS) systems due to their theoretically larger energy storage densities and efficiencies compared to sensible or latent storage [4, 8, 9]. Basic reaction schemes for TCS systems, including the CaO/Ca(OH)$_2$ reaction couple, were already proposed in 1976 [10] but they are still at a very early R&D stage from the point of view of their practical development and experimental study at pilot plant scale [10-17]:

$$CaO_{(s)} + H_2O_{(v)} \leftrightarrow Ca(OH)_{2\ (s)} \qquad \Delta H^o_{298K}=-109\ \text{kJ/mol} \qquad (1)$$
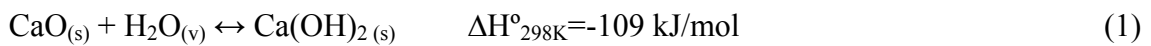
This chemical loop is based on two steps: first the CaO is hydrated in the presence of H$_2$O$_{(v)}$ and useful heat (i.e. at high temperature for efficient use in a steam cycle) is released from the exothermic reaction (discharge). The solid is then regenerated during the dehydration step (charge) by providing heat for the endothermic reaction (i.e. from the solar field) [11, 12]. In a previous work [16] we proposed a chemical process scheme for each of the charge/discharge steps of the CaO/Ca(OH)$_2$ storage system. The

scheme was based on a single fluidized bed (FB) reactor configuration alternating from hydration to dehydration conditions (at 470 and 550ºC, respectively, using $H_2O_{(v)}$ as both reactant and fluidizing gas) and two storage silos feeding/receiving solids to/from the FB. Decoupling of the reactions from the storage silos is essential to allow this process scheme to be used in large-scale applications, as it would be extremely challenging to arrange for vast heat transfer surfaces to manage the heat flows in large-scale stationary reactors containing all the solids of the storage system.

Other authors are considering the use of fixed/moving beds as their reference reactor for the hydration and dehydration steps [18-23]. In principle the use of FB reactors offers significant theoretical advantages when compared to fixed/moving beds because the larger heat transfer coefficients of fluidized beds [24] significantly reduce the heat transfer surface for the energy charge and discharge steps. The pressure drop for high gas velocities are reduced in a fluidized bed, and these can represent a serious weakness in large-scale fixed bed reactors requiring large gas flow rate inputs/outputs as it is the case in $CaO/Ca(OH)_2$ systems designed for energy storage applications.

For the single FB reactor configuration proposed and analyzed in a previous work [16] a heat transfer fluid (HTF), such as a molten salt is required in order to transfer the useful heat from the solar field to the storage system during the dehydration step and from the FB reactor to the steam cycle during hydration. Other configurations could be based on the use of dense particle suspensions as HTF to allow higher temperatures in the receiver [25-28] or even to directly dehydrate the solids in the solar receiver, as has been proposed by some authors for calcining $CaCO_3$ [29-31]. For the purpose and scope of this work, which is focused on reactor performance, we shall assume that a certain power input (Q_{IN}) coming from the solar field supplies the power necessary to reach the temperature of dehydration, trigger the endothermic reaction and, depending on the

amount of Q_{IN} available, provide additional power to further heat up the solids to temperatures above that of dehydration. During the discharge step, the sensible (Q_{OUTs}) and chemical heat (Q_{OUTr}) from the hot solids stored are used to preheat, vaporize and reheat the steam of the power cycle before the material is sent to the cold solids storage silo [16]. The sensible heat could be recovered by means of several fluidized bed heat exchangers (FB HX). These FB HX could be arranged in several series steps or in the form of elongated fluidized beds as described by Schwaiger et al. [32] for other solar applications. Other alternative configurations such as moving bed heat exchangers are already commercially available [33] and used at large scale [34].

A more detailed investigation of this energy storage system and its thermal integration within the solar field and steam power cycle is being investigated as part of the FP7 Storre project (www.storre-project.eu) but is beyond the scope of this work. The present study is focused on the performance of the gas-solid reactor and on the hydration and dehydration reactions in the fluidized beds of Figure 1. To our knowledge, only one other paper with a similar approach by Pardo et al. has been published to date [17]. Their study reported positive results for hydration and dehydration performance using very fine particle materials in the reactor (micrometric $CaO/Ca(OH)_2$ particles), low superficial gas velocities (around 0.1 m/s) and low temperatures and $H_2O_{(v)}$ partial pressures. In this work, our objective is to demonstrate the viability of FB reactors under more realistic operating conditions in a 5.5 kW testing batch bubbling fluidized reactor located at CEA-Grenoble, using high fluidization velocities, high $H_2O_{(v)}$ partial pressures and temperatures above 400ºC for both hydration and dehydration. A standard bubbling reactor model is employed to assist in the interpretation of the experimental results.

2. Experimental section

2.1. Experimental setup

The experimental set up used to study the hydration and dehydration reactions is based on a bubbling FB batch reactor, as shown in Figure 2. Significant improvements have been introduced into the facility with respect to a previous description of the set up [17], to allow it to operate at conditions relevant to large-scale systems. It has also been redesigned to be able to operate in the bed at temperatures up to 500ºC, total pressures slightly above the atmospheric, fluidizing gas velocities of up to 1 m/s (depending on the water vapour and air mixture introduced into the bed), inlet $H_2O_{(v)}$ partial pressures from 0 to 0.85, solids inventories between 1.5 to 3.5 kg and particle diameters (dp) between 100 and 800 μm.

The reactor consists of a cylinder made of stainless steel 316L. The column has an internal diameter of 0.105 m and is 0.9 m high. The gas distributor is made of a grid of 21 drilled screws. At the top of the bed, a 0.55 m high conical expansion prevents excessive slug expansion and solids entrainment. A 5.5 kW electrical oven (labelled as Electric Heater 2 in Figure 2) is used to heat the bed up to a maximum temperature of 500ºC and provides the chemical heat required for the reaction during dehydration. Improvements to the reactor electric heaters have been made in order to try to reduce heat losses in the experimental set up. Three electric heaters (Electric Heater 1, 3 and 4 in Figure 2) have been added in order to keep the reactor walls at temperatures above 300ºC. The maximum amount of electric power delivered to the overall system is 10.5 kW.

The temperature inside the bed (T_B in Figure 2) is measured at different positions by placing 1 mm K type thermocouples (200-500 ± 2ºC) in the center of the bed (r/R=1) at bed heights of 40, 140, 240 and 340 mm. Two more thermocouples located at height

240 mm and r/R=1/3 and r/R=2/3 make it possible to confirm whether temperature profiles are present within the bed of solids. The reactor temperature is controlled by a thermocouple located at a bed height of 240 mm. The temperature in the wall of the four electric heaters is measured using several thermocouples located at different points (not shown in Figure 2 for the sake of simplicity).

Upstream of the reactor, two separate circuits supply air and/or H_2O for the reactions to take place (see left-hand side of Figure 2). Flow meters are used to control the supply of liquid water (mini Cori-flow Bronkhorst 0-5 ± 0.012 kg/h) and dry air (Brooks 5853S 0-20 ± 0.016 Nm^3/h). The liquid water and the dry air are mixed before entering a 8.4 kW water vapour generator. The gas from the water vapour generator is further heated up before it enters the reactor bed. A bypass valve located before the reactor bed allows the reactor to be prepared for each experiment. Firstly, the circuits and filters are preheated and dried with air before testing begins. Then, when the desired testing temperature has been reached, the gas mixture coming from the water vapour generator bypasses the reactor in order to stabilize the hygrometers signal. Two 90-liter filters boxes are located after the reactor in order to remove the finer particles elutriated by the gas before they leave the system.

The conversion of the solids is followed during testing by conducting a mass balance of the water mass flowrate (m_{H2O}) between the inlet and outlet of the reactor. The m_{H2O} at the outlet of the reactor is measured by two capacitive hygrometers HC2-HC102 from ROTRONIC (0-100 ± 2.39%HR, 20-200 ± 0.2ºC). One of the hygrometers is located just after the reactor and the other after the filters (HYG1 and HYG2 respectively in Figure 2). HYG1 was found to be the more reliable hygrometer in most of the tests due to its faster response. The signal given by HYG2 is only qualitative compared to that of HYG1 (to determine whether the behavior of HYG1 is correct at any given time). In any

case, an internal re-calibration of the signal of the hygrometers is applied in every experiment to match the input and output signals of the hygrometers when no reaction is taking place in the bed.

2.2. Experimental procedure

In a typical test, between 1.5 to 3 kg of commercial pre-calcined lime (95%wt CaO obtained from the calcination of $CaCO_3$ at 1000ºC, as supplied by Carmeuse) is heated up in the reactor to working conditions. Due to the thermal inertia of the system this operation takes around one hour. A matrix of the initial experimental conditions has been generated taking into account the following experimental variables: the initial temperature of the fluidized bed (between 390-460ºC for hydration and 450-500ºC for dehydration), the granulometry (200-400 µm) and mass of lime material (between 1.8-2.5 kg), the $H_2O_{(v)}$ partial pressure (between 0.57-0.84 for hydration and 0-0.08 for dehydration) and the fluidizing velocity (between 0.3-0.5 m/s).

Once the parameters mentioned above have been selected, the system is operated in bypass mode until the initial temperatures and flow rates reach a steady state. Once the system is in steady state with no reaction taking place, the bypass valve is switched off to allow the reacting mixture of gases to enter the fluidized bed. The end of each experiment is detected by both the signal of the heat power delivered to the bed and the signal of the hygrometers, as will be shown in more detail in section 3.2. Typically, each test campaign consists of a few cycled series of dehydration and hydration reactions under different operation conditions. After the testing campaign, each batch of material is discarded.

2.3. Material characterization

The commercial lime batch was sieved to different particle sizes (100-200 μm, 200-400 μm and 400-600 μm and 600-800 μm). The test campaigns described in this work were carried out using a batch with a particle size range of 200-400 μm. Crushing strength values of 5 N (measured by a SHIMPO FGE-5X dynamometer supported on a SHIMPO MFGS-100L manual test stand) confirmed that this material could be used for a few hydration/dehydration cycles in the experimental facility without generating, during hydration, a very large fraction of fines characteristic of other lime materials calcined at lower temperatures [35].

The reactivity of the CaO material towards the hydration and dehydration reactions was measured using a thermogravimetric (TG) equipment described in detail elsewhere [35]. This information will be fed into the reactor model used to discuss the experimental results. The system is based on a TG analyzer coupled to a water vapour generation line that is able to provide a steady flow of pure $H_2O_{(v)}$ or air/$H_2O_{(v)}$ mixtures. The CaO sample in a platinum sample hangs in a 2.5×10^{-2} m quartz tube located inside an oven that can reach temperatures of up to 1000ºC. Through the bottom of the quartz tube the reaction gases (H_2O and/or air) are introduced at high velocity (0.05 m/s at 500ºC around the sample) to avoid external mass transfer resistances. The generation of a stable flow of $H_2O_{(v)}$ in this system is possible thanks to a pipe heated up to 400ºC into which a measured flow of liquid water is fed from pressurized tanks. Several filters and a pneumatic valve located in the heated up pipe facilitate a uniform and steady flow of $H_2O_{(v)}$ during the TG tests. Around 3 mg of sample was employed for these TG tests in order to extract kinetic information at particle level for use in the reactor model (see sections 3.3 and 3.4).

3. Results and discussion

3.1. Description of a typical test

A typical dehydration and hydration reaction cycle is shown in Figure 3, where some of the main variables measured during the tests are plotted vs time. The average heat power supplied by the heater located around the bed of solids is represented in Figure 3a (Electric Heater 2 in Figure 2), where around 3-4 kW are delivered to the bed during the endothermic reaction, whereas no heat power is required for the exothermic reaction as one might expect. In relation to the gas flows at the inlet and outlet of the reactor (Figure 3b), some discrepancies between the signal measured by the hygrometers and the input flow of $H_2O_{(v)}$ when no reaction is occurring were detected. In such cases, an internal re-calibration is applied, as shown in Figure 3b, by setting the exit mass flow of $H_2O_{(v)}$ at the end of the experiment (when the reaction has run its course) equal to the $H_2O_{(v)}$ inlet mass flow .

Other important measurements include the temperatures at the center of the bed (Figure 3c) and at the walls of the four heaters (Figure 3d). As can be seen, there is a good agreement between the thermocouples T_{B1} to T_{B5} located inside the bed at different axial and radial positions (see Figure 2 for details) indicating a good mixing of the solids. The difference observed in the case of T_{B6} is due to the fact that the fluidizing solids do not reach this thermocouple (as it is 340 mm from the distributor). In other tests performed with a higher mass of solids there is good agreement between the 6 thermocouples inside the bed. In contrast, the wall temperatures of the heaters (Figure 3d), show significant differences (TW1 vs TW2). These discrepancies can be explained by taking into account that they are not located at the same position and also they can be disturbed by the heater wires.

The test corresponding to Figure 3 proceeds in bypass mode for the first 7 minutes of data recording before dehydration begins to give the system time to heat up while the bed remains unfluidized. At min 7 the bypass is switched off in order to feed the pre-arranged gas flow mixture to the bed (in this case 6 Nm^3/h of air with no water vapour, at a temperature set to 500ºC and a target gas velocity, $u_{TBed\ in}$, of around 0.5 m/s). As soon as the air flow enters the reactor, the solids begin to dehydrate and the signal given by the hygrometers increases from 0 to a maximum of around 0.75 kg/h of $H_2O_{(v)}$ (Figure 3b). A peak for the water vapour flow is recorded by the hygrometer HYG2 at the very beginning of the experiment. This peak has also been observed in other testing conditions and is attributed to the water vapour accumulated in the system in some tests were the bypass time before dehydration was not long enough as to eliminate all the steam present in the system elements located after the reactor (i.e. the large filters). This experimentally observed effect on the HYG2 signal also supports the selection of HYG1 (just after the reactor) as the more reliable hygrometer. The end of the dehydration reaction is confirmed by both the signal from the hygrometers (a sharp decrease in $m_{H2O,\ out}$ towards zero at around 30 min in Figure 3b) and the heat power delivered to the bed at the same point in time in Figure 3a. This figure also shows that there is a sharp increase in heat power supplied to the bed at the beginning of the experiment, as this is necessary to maintain the temperature at 500ºC during the endothermic dehydration reaction. The need for this power input decreases sharply as dehydration comes to an end at around 30 min. After dehydration is completed, the temperature of the reactor is allowed to move towards the conditions for hydration, which starts at min 67. For the hydration reaction shown in Figure 3 the gas mixture consists of 3 kg/h of $H_2O_{(v)}$ and 3 Nm^3/h of air (equivalent to an inlet $H_2O_{(v)}$ partial pressure, $v_{H2O,in}$, of 0.57) and the initial reactor temperature is fixed at 400ºC ($u_{TBed,\ in}$ of

0.43 m/s). As the mixture of water vapour and air enters the reactor, the outlet flow of $H_2O_{(v)}$ is negligible for a few minutes as most of it is consumed by the hydration of the solids. As a consequence of the exothermic reaction, the temperatures of the bed and heaters around the reaction area increase (see Figure 3c and the TW1 and TW2 of Heater 2 in Figure 3d). As expected, in the hydration reaction, the electric power required to maintain the reactor temperature becomes zero as the exothermic hydration reaction is sufficient to compensate for heat losses during this period and to satisfy the energy requirements for heating up the gas entering the reactor. As the conversion of the solids and their temperature increase (no means of refrigerating of the bed are available) the hydration reaction slows down because the conditions get closer and closer to equilibrium. As in the case of dehydration, the $m_{H2O,in}$ and $m_{H2O,out}$ values are continuously monitored and the end of the hydration reaction (at around min 92) is established both by the signal from the hygrometers (when $m_{H2O,out}$ approaches $m_{H2O,in}$) and by a rapid decrease in the bed temperature (indicating the virtual end of the exothermic hydration reaction), as can be appreciated in Figures 3c and 3d. Indeed, at around 103 min in this example, when the hydration reaction has finished, the electric power supply (Figure 3a) is again required to maintain the bed temperature at the pre-set set point and to compensate for heat losses.

3.2. Experimental results

Following the procedure described above, several tests were performed to study the effect of the mass of CaO material in the bed, the gas velocity, the $H_2O_{(v)}$ partial pressure and the temperatures upon the hydration and dehydration reactions in the FB experimental set up. Tables 1 and 2 contain the most relevant operation conditions for selected hydration and dehydration tests. Key experimental variables for assessing reactor performance such as the maximum solids conversion achievable by the solids

loaded into the bed (X_{max}) which determines the initial moles of active material inside the bed ($N_{Ca\ active} = N_{Ca\ total} \cdot X_{max}$) and the experimental reaction times (t_{exp}) measured for each batch of solids are also included in Tables 1 and 2. As was established in the TG tests (see section 3.3.), the CaO material tested in this work yielded X_{max} values between 0.2-0.4 (as a result of the severe calcination conditions to which the $CaCO_3$ precursor was subjected in order to give the resulting material sufficient mechanical strength). Tables 1 and 2 also contain the equilibrium $H_2O_{(v)}$ partial pressure at two relevant experimental temperatures of each experiment. In the case of the hydration tests (Table 1), the experimental maximum temperature reached by the bed ($T_{Bed,\ max}$ at about 480ºC in Figure 3c) is also shown. Note that for most of the tests performed so far there is an increment of between 40-90ºC with respect to the initial temperature during the hydration test.

As can be seen from the data in Table 1, most of the hydration tests in the batch reactor under the operation conditions selected lasted between 18 and 28 min. However, substantially longer hydration times were measured for experimental tests nº 1-3. For these two tests, the conditions were considerably closer to equilibrium (as a consequence of the high increase in bed temperature during testing and the low input gas velocities). This made the overall reaction go slower and so the reaction times were almost three times longer than in the other tests. The slightly lower reaction time of test nº 1 compared to test nº 2 can be attributed to the higher operation temperature, which favors faster hydration reaction rates for a similar difference between the input and equilibrium $H_2O_{(v)}$ partial pressure. On the other hand, longer reaction times are measured as the bed temperature is considerably increased along the hydration reaction (i.e. T_{Bed} around 500ºC along test nº 3). If the temperature of the bed could be maintained at a lower $T_{Bed,\ max}$ (by extracting heat from the bed) the reaction time

necessary to achieve the maximum solids conversion would be shorter, as in the case of tests nº 4 and 5.

The effect of the active mass of Ca can be appreciated by comparing tests nº 6, 7 and 8 at the same gas velocity and similar differences between the input and equilibrium $H_2O_{(v)}$ partial pressures. As expected, as $N_{Ca\ active}$ increases the hydration reaction time also increases. Longer reaction times can be expected for test nº6 compared to tests nº 7 and 8, as the mol of active material is almost doubled in test nº 6. However, it is worth noting that the evolution of the bed temperature during the hydration tests can fluctuate slightly from one test to another. Differences of around 10ºC (as in the case of these tests) can have a significant impact on the reaction rates as we are operating at conditions close to equilibrium. Finally, in tests nº 9 and 10 the effect of the $H_2O_{(v)}$ partial pressure and the temperature of the bed are studied. In test nº 9 a greater difference between the input and equilibrium $H_2O_{(v)}$ partial pressure was observed as a consequence of the smaller increase in bed temperature. This effect, combined with the slightly higher gas velocity, reduces the reaction time of test nº 9 considerably compared to test nº 10 for a similar amount of active material.

In addressing the experimental conditions and results compiled in Table 2 for dehydration experiments, it must be borne in mind that due to certain limitations in the experimental facility (a limited maximum temperature) we were forced to perform most of the dehydration tests under a low $H_2O_{(v)}$ partial pressure (<0.1). Furthermore, for the same reason, control of the bed temperature during dehydration was difficult in some of the tests as the bed temperature tended to decrease as a consequence of the endothermic dehydration reaction (in some cases by as much as 50ºC, see $T_{Bed,in}$ and $T_{Bed,min}$ in Table 2).

Despite these limitations to temperature control, the experiments provided valuable information for model validation purposes. Some tests performed under a low $H_2O_{(v)}$ partial pressure at the inlet revealed clearly the effect of the bed temperature over the experimental times (see tests nº 11-13 with decreasing t_{exp} as $T_{Bed,min}$ increases). As expected, when no water vapour is introduced to the bed and the gas velocity is kept high enough to ensure that $v_{H2O,out}$ is far from equilibrium, the dehydration reaction is relatively fast and reaction times can be reduced (as in test nº 15 compared to test nº 12). In contrast, reaction times are longer as the gas velocity decreases and the amount of active material inside the bed increases (see tests nº 16 and 17). The effect of the mass of active material is further evaluated in tests nº 18-20, where extended dehydration times are needed as the mass of active material increases, while the rest of the operation conditions are maintained.

In general, the results shown in Tables 1 and 2 are in qualitative agreement with the expected effects of the different variables studied in this work upon the hydration and dehydration reactions in the experimental set up based on the $CaO/Ca(OH)_2$ equilibrium. However, to ensure a more rigorous evaluation of these trends, a basic bubbling batch reactor model was adapted to the conditions of the experiments of this study.

3.3. Basic reactor model

The reactor model developed in this work for the hydration of CaO and the dehydration of $Ca(OH)_2$ is a classic bubbling bed model [24] schematically shown in Figure 4. The figure represents two cases, in which there is an axial profile of partial pressure of water vapour in the bubbling phase (free of solids) as a result of the gas-solid reactions taking place in the emulsion phase (assumed to be minimum fluidization conditions). A certain exchange of gas is allowed between the bubble and emulsion phase. The objective of

the reaction model is to estimate the axial profile of the partial pressure of water vapour in the reactor that will determine the water vapour concentration at the exit of the reactor and hence the overall reactor efficiency during hydration and dehydration. This can be then compared with and validated against the experimental results discussed in previous sections.

The model is solved assuming plug flow (PFR) for the gas in the bubble phase and perfect mixing (CSTR) of the gas and solids ($v_{H2O,e}$ constant along Z in the emulsion phase for a given time t_i). Bubbling properties and their related model parameters are considered to be constant despite the changes that take place in the reactor with time (such as solids conversion) and location (as water vapour appears or disappears from the gas phase, generating changes in phase volume fractions, as indicated in Figure 4). These assumptions are a simplification consistent with the level of experimental information available (i.e. no experimental information on axial concentration profiles or changes in bubble properties is available). For larger reactor beds operated in pure $H_2O_{(v)}$ and/or very active materials, the changes in fluid volume as consequence of the variation in the total molar flow due to the reaction should be taken into consideration, as they will have an influence on hydrodynamics of the bubbles, especially in beds of small particles [36]. It is also assumed that the gas in excess of what is required for incipient fluidization passes through the bubbles (which are of uniform size) and that each bubble exchanges gas with the emulsion phase as it rises. There is no gas-solid reaction in the bubbles, only in the emulsion phase.

Furthermore, a key assumption for solving the model involves the simplifications needed to avoid having to formulate the bubbling model in dynamic conditions where bed characteristics change with time (i.e. having to account for the change in conversion with time as the conversion of the solids progresses towards full hydration or

dehydration conditions and the end of the reaction leading to the complete conversion of the solids). It can be assumed that during the short time relevant for the gas passing through the bed (of the order of one second) the change in the conversion of the solids is negligible and the gas sees a bed of constant solid properties (pseudo-stationary state assumption). As mentioned below, an overall mass balance of the reactor over time can be applied to correct the solids conversion over time.

For the sake of conciseness, the mass balances of the model are described below only for the hydration step, as the same procedure can be applied for dehydration, by merely changing the sign of the reacting flows of $H_2O_{(v)}$. For a given set of bed characteristics at a certain time t_i (input variables of Figure 4 and an average solids hydration conversion achieved at a time t_i) the mass balance for the water vapour in a control volume of the complete reactor (in molar flows of $H_2O_{(v)}$) can be written as follows:

$$F_{H2O,Hy\ in} - F_{H2O,Hy\ out} = N_{Ca\ active} \cdot r_{Hy,e} \tag{2}$$

where the term $r_{Hy,e}$ is given by the reaction kinetics of the material in the emulsion environment (assumed to be well mixed for gas and solids):

$$r_{Hy,e} = k_{Hy}^{2/3}(v_{H2O,e} \cdot v_{H2O,eq})(1-X_{Hy}) \tag{3}$$

k_{Hy} being the effective kinetic constant of the material reacting in the emulsion phase.

The solution of the mass balance (2) requires the calculation of the partial pressure of $H_2O_{(v)}$ in the emulsion, $v_{H2O,e}$, which depends on the intensity or efficiency of the gas exchange between the bubble and emulsion phases (i.e. the cross flow factor, X_{factor}, from the Davidson and Harrison [37] model for a two-phase fluidized bed). Low values

of X_{factor} indicate that more gas tends to bypass the reactor through bubbles without reacting, while a high X_{factor} value implies a high rate of gas interchange between phases. Therefore the X_{factor} is used here to link the $H_2O_{(v)}$ partial pressure in the bubble and emulsion phases, $v_{H2O,b}$ and $v_{H2O,e}$ respectively through the following mass balance [37]:

$$-V_b u_b \left(dv_{H2O,b} / dz \right) = (q_b + k_G S_b)(v_{H2O,b} - v_{H2O,e}) \tag{4}$$

where u_b represents the bubble rising velocity and q_b and k_G the convective throughflow in and out of the bubble and the mass transfer between the main volume of the bubble (with $v_{H2O,b}$) and the bubble walls (with $v_{H2O,e}$) respectively for a bubble of volume V_b and surface area S_b. These terms can be related with the interchange coefficient [24], $K_{be}=(q_b+k_GS_b)/V_b$, as follows:

$$-dv_{H2O,b} / dz = \left(K_{be} / u_b \right)(v_{H2O,b} - v_{H2O,e}) \tag{5}$$

Integrating equation (5) between 0 and Z and using the boundary condition $v_{H2O,b}=v_{H2O,b0}=v_{H2O,\,in}$ at Z=0 gives:

$$v_{H2O,\,bz} = v_{H2O,e} + (v_{H2O,\,b0} - v_{H2O,e}) \exp(-X_{factor}) \tag{6}$$

where the dimensionless cross flow factor can be related with the Kunii-Levenspiel interchange coefficient [24], K_{be} as follows:

$$X_{factor} = (K_{be} Z) / u_b \tag{7}$$

The $H_2O_{(v)}$ partial pressure at the outlet ($v_{H2O,Z}=v_{H2O,out\,at\,Z=1}$) can be calculated with a mass balance to estimate the average concentration in the bubble and emulsion phases:

$$v_{H2O,z} = v_{H2O,e} \cdot \left(u_{mf} / u \right) + v_{H2O,bz} \cdot \left((u - u_{mf}) / u \right) \tag{8}$$

and related with the outlet molar flow of $H_2O_{(v)}$ as follows:

$$P_{H2O,Hy\ out} = \frac{(F_g \cdot v_{H2O,z})}{(1 - v_{H2O,z})} \tag{9}$$

Finally, in order to correct the solids conversion over time, the overall mass balance of the reactor is considered:

$$X_{Hy,ti} = X_{Hy,ti-1} + \frac{(P_{H2O,Hy\ in} - P_{H2O,Hy\ out})}{N_{Ca\ active}}(t_i - t_{i-1}) \tag{10}$$

At each time t_i the model is iteratively solved in order to find the values of $F_{H2O,\ Hy\ out}$ and $v_{H2O,e}$ that will make equations (2-10) met. To solve the model several variables characteristic of each experiment are required as input data: the initial moles of active Ca inside the reactor ($N_{Ca\ active}$), the inlet molar flows of steam and inert gas ($F_{H2O,\ in}$ and F_g respectively) and the temperature inside the bed (T_{Bed}). Information and kinetic parameters related to the hydration and dehydration reactions are also required. As can be seen from equation (3) we have modeled the reactions as a shrinking core model as in a previous work [35] where values for the pre-exponential factor of 2.5×10^{-6} and 5.2×10^2 s^{-1} (for a particle size of 100−200 μm) and activation energies of 59.4×10^3 and 60.8×10^3 J/mol for hydration and dehydration respectively were obtained. However, these results were obtained in tests using CaO materials of very high inherent reactivity (i.e. high surface area). Also, complete conversion was measured for those reference CaO materials (obtained from the calcination of $CaCO_3$ at 850ºC, as described in [35]). In contrast, the materials used for the pilot in this study were commercial "overburned" lime materials (obtained from the calcination of $CaCO_3$ at around 1000ºC) of lower reactivity and higher mechanical strength chosen to minimize attrition losses during the experiments. Therefore, a re-evaluation of the kinetic parameters of these materials was necessary using the thermogravimetric equipment and methodology described elsewhere for more reactive lime samples [35]. TG hydration and dehydration tests of the CaO material (as received) and also cycled samples from experiments from the

reactor pilot plant were carried out at temperatures between 400-550ºC and at different $H_2O_{(v)}$ partial pressures ranging from air to pure $H_2O_{(v)}$. Significantly, a maximum hydration conversion of only 0.2-0.4 was recorded for all these CaO materials that already showed substantial mass transfer limitations at particle level to the progression of the hydration reaction as a $Ca(OH)_2$ layer is formed on free surfaces of CaO (that are known to decrease with increasing calcination temperatures). It is beyond the scope of this study to analyze in detail the mechanism behind this change in reactivity of CaO as the calcination temperature of the precursor increases, but these results highlight the importance of using reliable kinetic parameters in the reactor model.

Examples of typical thermogravimetric results using bed material are shown in Figure 5 including the best fit curves for the kinetic model described elsewhere adapted to accept a different pre-exponential factor but the same activation energies. For the conversion shown in Figure 5 the moles of active CaO are used, taking into account the lower maximum conversion values measured for this material (X_{max} between 0.2-0.4).

The results of Figure 5a indicate that the hydration of the materials used in the reactor test evolves at a rate which is about 1/5 of that of the hydration test of the reference CaO materials used in a previous work [35]. In contrast, the dehydration part of the cycles (Figure 5b) revealed rates of dehydration fully consistent with the reference materials (i.e. with the same pre-exponential factor and deactivation energies). Although these findings do not come within the scope of this paper, they indicate that the mechanism of dehydration is much less sensitive to the textural properties of the dehydrating material. Nevertheless, these kinetic parameters for hydration and dehydration reactions have been introduced into the reactor model described above for the final validation of the model against the experimental results described in section 3.2.

3.4. Reactor model validation

Predictions given by the reactor model described in section 3.3. have been compared with the experimental results to assist in the interpretation of the results obtained from the facility. As mentioned above, the reactor model requires only one single adjustable parameter to characterize the bubble-emulsion mass transfers, the X_{factor}. The remaining input parameters for each test are experimental conditions: $N_{Ca\ active}$, $F_{H2O,\ in}$, F_g and T_{Bed}. The T_{Bed} evolution with time is introduced to the model as an input data from experimental measurements. The evolution of T_{Bed} in an adiabatic reactor could be estimated from a heat balance of the reactor to account for the reaction enthalpies and input and output flow of gases. However, such a heat balance would be too complex for this particular facility as it would be necessary to estimate for the setup of Figure 2 heat losses, the thermal inertia of the reactor, bed, refractories and instruments, etc.

Figures 6 and 7 show experimental curves representing the molar $H_2O_{(v)}$ flow measured at the outlet of the reactor (dots) and the predictions given by the model (lines) described above for some selected tests of hydration and dehydration shown in Tables 1 and 2. In all cases, a single cross flow factor of 1.5 has been applied to fit the experimental results shown in Figures 6 and 7. As can be seen, there is a good agreement between the experimental results even with this simplified model when using this single parameter. The low X_{factor} value required compared to others reported for other reactor systems (typically around 3 [37]) indicates a relatively poor gas exchange efficiency between the bubble and emulsion phases during the tests performed in this experimental facility.

In the case of the hydration reaction, it is possible to fit the results using the same X_{factor} ~ 1.5, but any $X_{factor} > 1.5$ can be also used to obtain a marginally better fit. This is a clear indication that the relatively slower hydration kinetics under these test conditions and for this material (see Figure 5) is controlling the overall process of the reaction in

the reactor and that the bubble-emulsion mass transfer resistances can be ignored. Furthermore, as shown in Figure 6, during most of the hydration test (except for the first 2-3 minutes of the test), the change in molar flow of $H_2O_{(v)}$ between the inlet and outlet is very low. This means that during hydration the FB reactor approaches to a differential reactor with only small changes in the water vapour concentration inside the bed which means that $v_{H2O,e}$ is close to $v_{H2O,b}$.

In contrast, the effect of the mass transfer resistance represented by the cross flow factor during dehydration is much more noticeable. As highlighted in section 3.3, the dehydration reaction was found to be faster than hydration under equivalent operation conditions (i.e. close to equilibrium). However, at the high gas velocities of the experimental tests described in this work, the large bubbles that can be expected in the bed during dehydration (growing in size) will not favor the mass transfer between phases and could also induce slugging or other effects that will reduce effective contact between the bubbles and the emulsion during the fast dehydration reaction. The low cross flow factor needed to fit the results indicates that the particles in the emulsion phase will be surrounded by a richer atmosphere of water vapour ($v_{H2O,e}>v_{H2O,b}$) resulting from the dehydration of the solids in the emulsion phase, that will make their reaction rate proceed more slowly. In addition, we can speculate on an additional mechanism to explain the relatively low values of X_{factor} needed to fit the dehydration results: the gas exchange mechanism to transport fresh air from the bubbles to the surroundings of the particles, thereby reducing the partial pressure of $H_2O_{(v)}$ around the particles, will meet during dehydration a net flow of gas (the $H_2O_{(v)}$ resulting from dehydration) flowing from the opposite direction. The overall effect will be a lower driving force for the transfer of gas from the bubble (diluted in $H_2O_{(v)}$) to the emulsion phase.

To illustrate the impact of the X_{factor} as a fitting parameter for the reactor results during hydration and dehydration we carried out a sensitivity analysis as shown in Figure 8 where different calculated $F_{H2O, out}$ curves vs time have been plotted for different X_{factor} values. For this sensitivity analysis the temperature in the reactor was assumed to be constant with time. As can be seen, during hydration the effect of the X_{factor} is less pronounced as a consequence of strong kinetic control of the relatively slow hydration rates of the particles in the bed. In contrast, the fast intrinsic dehydration reaction is greatly influenced by the X_{factor} values, which is consistent with the large mass transfer control reflected in the experimental results. In this case, in comparison with the predicted dehydration times, differences of around 14 min for X_{factor} values between 0.5 and 5 are observed (compared to only 4 min for the hydration reaction).

The high mass transfer limitations detected during some of the reactor tests described in this work need to be put in context when applied to conditions in large scale systems, where both hydration and dehydration reactions will probably be performed under steady state conditions with a high concentration of $H_2O_{(v)}$ in continuous reactors [16]. Work is ongoing to build a continuous pilot plant within the framework of the Storre project to test these conditions. Nevertheless, the model discussed in this paper provides a basis for scaling up the results of this study to more realistic conditions in future large scale $CaO/Ca(OH)_2$ energy storage systems.

4. Conclusions

The $CaO/Ca(OH)_2$ hydration/dehydration reaction for future energy storage systems has been successfully investigated in a batch fluidized bed operated at high gas fluidization velocities (0.3-0.5 m/s), temperatures of around 400-500ºC and $H_2O_{(v)}$ partial pressures of up to 0.84. Valuable information has been obtained for validating a standard bubbling reactor model by using just one single parameter, the cross flow factor, to model the

experimental results obtained. Kinetic information at particle level obtained from TG tests was needed by the model to derive coherent cross flow factors of around 1.5. Hydration reaction rates were found to be 5 times slower than the reference CaO (as a consequence of the severe calcination process undergone by the samples), while the dehydration kinetics was of the same order of magnitude as the highly active reference CaO materials used in previous works. Once these kinetics data have been taken into account, the model fits well to the experimental hydration results with cross flow factors higher than 1.5 as the slow kinetics controls the reaction inside the bed. On the other hand, a relatively large bubble-emulsion mass transfer resistance was observed in the dehydration test (cross flow factor values of around 1.5 were required to fit the results). Although more experimental studies are required (in particular in future continuous pilot units) the current level of validation provided by the model offers encouraging support for the scaling-up of bubbling fluidized bed reactors for thermochemical energy storage applications based on the $CaO/Ca(OH)_2$ reversible reaction loop.

Nomenclature

dp particle size, μm

F_g molar flow of fluidizing gas (i.e. air), mol/s

F_{H2O} molar flow of $H_2O_{(v)}$, mol/s

k kinetic constant, s^{-1}

K_{be} interchange mass transfer coefficient between bubble and emulsion, s^{-1}

k_G mass transfer coefficient between bubble and emulsion, m/s

M_{CaO} mass of total solids, kg

m_{H2O} mass flow of $H_2O_{(v)}$, kg/h

$N_{Ca\ active}$ moles of active Ca material, mol

$N_{Ca\ total}$ moles of total Ca material, mol

q_b volume flow-rate in and out of the bubble, m^3/s

Q_{Air} volumetric air flow, Nm^3/h

S_b bubble surface area, m^2

t reaction time, s

T temperature, ºC

t_{exp} experimental testing time, min

u input gas velocity, m/s

u_b velocity of the rising bubbles, m/s

u_{mf} velocity at minimum fluidization conditions, m/s

V_b bubble volume, m^3

X conversion of active material, mol H_2O/mol CaO active

X_{factor} cross flow factor

Z solids bed height, m

Greek symbols

ΔH^o reaction enthalpy, kJ/mol at 298K

v_{H2O} $H_2O_{(v)}$ partial pressure

$v_{H2O,eq}$ equilibrium $H_2O_{(v)}$ partial pressure

$v_{H2O,Z}$ $H_2O_{(v)}$ partial pressure at bed height Z

Subscripts

b   bubbles

Bed   bed of solids

Dehy   dehydration reaction

e   emulsion

Hy   hydration reaction

In   initial/input conditions

Max   maximum value

Min   minimum value

Out   outlet conditions

Ref   reference CaO material

Acknowledgements

References

[1] IPCC, Climate change 2014: Synthesis report. Contribution of Working Group I, II and III to the Fifth Assessment Report of the Intergovernmental Panel on Climate Change, International Panel on Climate Change, Geneva, Switzerland, 2014.

[2] IRENA, REthinking energy: Renewable energy and climate change, International Renewable Energy Agency, United Arab Emirates, 2015.

[3] IEA, Technology roadmap: Energy storage, International Energy Agency, Paris, France, 2014.

[4] C. Prieto, P. Cooper, A.I. Fernández, L.F. Cabeza, Review of technology: Thermochemical energy storage for concentrated solar power plants, Renew. Sust. Energ. Rev. 60 (2016) 909-929.

[5] H. Zhang, J. Baeyens, G. Cáceres, J. Degrève, Y. Lv, Thermal energy storage: Recent developments and practical aspects, Prog. Energ. Combust. 53 (2016) 1-40.

[6] S. Kuravi, J. Trahan, D.Y. Goswami, M.M. Rahman, E.K. Stefanakos, Thermal energy storage technologies and systems for concentrating solar power plants, Prog. Energ. Combust. 39 (2013) 285-319.

[7] Y. Tian, C. Zhao, A review of solar collectors and thermal energy storage in solar thermal applications, Appl. Energ. 104 (2013) 538-553.

[8] P. Pardo, A. Deydier, Z. Anxionnaz-Minvielle, S. Rougé, M. Cabassud, P. Cognet, A review on high temperature thermochemical heat energy storage, Renew. Sust. Energ. Rev. 32 (2014) 591-610.

[9] J. Cot-Gores, A. Castell, L.F. Cabeza, Thermochemical energy storage and conversion: A-state-of-the-art review of the experimental research under practical conditions, Renew. Sust. Energ. Rev. 16 (2012) 5207-5224.

[10] W.E. Wentworth, E. Chen, Simple thermal decomposition reactions for storage of solar thermal energy, Sol. Energy 18 (1976) 205-214.

[11] G. Ervin, Solar heat storage using chemical reactions, J. Solid State Chem. 22 (1977) 51-61.

[12] G. Ervin, Method of storing and releasing thermal energy, Rockwell International Corporation, U.S. Patent 3,973,552 (1976).

[13] F. Schaube, L. Koch, A. Wörner, H. Müller-Steinhagen, A thermodynamic and kinetic study of the de- and rehydration of $Ca(OH)_2$ at high H_2O partial pressures for thermo-chemical heat storage, Thermochim. Acta 538 (2012) 9-20.

[14] D.R. Brown, J.L. La Marche, G.E. Spanner, Chemical energy storage system for solar electric generating system (SEGS) solar thermal power plant, J. Sol. Energ. Eng. 114 (1991) 212-218.

[15] J.K. Rosemary, G.L. Bauerle, T.H. Springer, Solar energy storage using reversible hydration/dehydration of $CaO\text{-}Ca(OH)_2$, in: AIAA Terrestrial Energy Systems Conference, Orlando, Florida, 1979.

[16] Y.A. Criado, M. Alonso, J.C. Abanades, Z. Anxionnaz-Minvielle, Conceptual process design of a $CaO/Ca(OH)_2$ thermochemical energy storage system using fluidized bed reactors, Appl. Therm. Eng. 73 (2014) 1089-1094.

[17] P. Pardo, Z. Anxionnaz-Minvielle, S. Rougé, P. Cognet, M. Cabassud, $Ca(OH)_2/CaO$ reversible reaction in a fluidized bed reactor for thermochemical heat storage, Sol. Energy 107 (2014) 605-616.

[18] A. Kanzawa, Y. Arai, Thermal energy storage by the chemical reaction augmentation of heat transfer and thermal decomposition in the $CaO/Ca(OH)_2$ powder, Sol. Energy 27 (1981) 289-294.

[19] I. Fujii, K. Tsuchiya, M. Higano, J. Yamada, Studies of an energy storage system

by use of the reversible chemical reaction: $CaO + H_2O \rightleftharpoons Ca(OH)_2$, Sol. Energy 34

(1985) 367-377.

[20] F. Schaube, A. Kohzer, J. Schütz, A. Wörner, H. Müller-Steinhagen, De- and rehydration of $Ca(OH)_2$ in a reactor with direct heat transfer for thermo-chemical heat storage. Part A: Experimental results, Chem. Eng. Res. Des. 91 (2013) 856-864.

[21] F. Schaube, I. Utz, A. Wörner, H. Müller-Steinhagen, De- and rehydration of $Ca(OH)_2$ in a reactor with direct heat transfer for thermo-chemical heat storage. Part B: Validation of model, Chem. Eng. Res. Des. 91 (2013) 865-873.

[22] M. Schmidt, C. Szczukowski, C. Roßkopf, M. Linder, A. Wörner, Experimental results of a 10 kW high temperature thermochemical storage reactor based on calcium hydroxide, Appl. Therm. Eng. 62 (2014) 553-559.

[23] J. Yan, C.Y. Zhao, Experimental study of $CaO/Ca(OH)_2$ in a fixed-bed reactor for thermochemical heat storage, Appl. Energ. 175 (2016) 277-284.

[24] D. Kunii, O. Levenspiel, Fluidization Engineering, 2nd ed., Butterworth-Heinemann, USA, 1991.

[25] J. Spelling, A. Gallo, M. Romero, J. González-Aguilar, A high-efficiency solar thermal power plant using a dense particle suspension as the heat transfer fluid, Energy Procedia 69 (2015) 1160-1170.

[26] B. Boissiere, R. Ansart, D. Gauthier, G. Flamant, M. Hemati, Experimental hydrodynamic study of gas-particle dense suspension upward flow for application as new heat transfer and storage fluid, Can. J. Chem. Eng. 93 (2015) 317-330.

[27] G. Flamant, M. Hemati, Device for collecting solar energy, U.S. Patent Appl. 2013/0284163 A1 (2013).

[28] G. Flamant, G. Olalde, High temperature solar gas heating comparison between packed and fluidized bed receivers—I, Sol. Energy 31 (1983) 463-471.

[29] S.E.B. Edwards, V. Materić, Calcium looping in solar power generation plants, Sol. Energy 86 (2012) 2494-2503.

[30] R. Chacartegui, A. Alovisio, C. Ortiz, J.M. Valverde, V. Verda, J.A. Becerra, Thermochemical energy storage of concentrated solar power by integration of the calcium looping process and a CO_2 power cycle, Appl. Energ. 173 (2016) 589-605.

[31] A. Imhof, Decomposition of limestone in a solar reactor, Renew. Energ. 10 (1997) 239-246.

[32] K. Schwaiger, M. Haider, F. Holzleithner, R. Eisl, sandTES-A novel thermal energy storage system based on sand, in: 21st International Conference on Fluidized Bed Combustion, Naples, Italy, 2012.

[33] N. Jordison, N.A. Rozendaal, P. Xingeun Huang, Indirect-heat thermal processing of particulate material, U.S. Patent 8578624 B2 (2013).

[34] K. Kim, Y. Son, W.B. Lee, K.S. Lee, Moving bed adsorption process with internal heat integration for carbon dioxide capture, Int. J. Greenh. Gas. Con. 17 (2013) 13-24.

[35] Y.A. Criado, M. Alonso, J.C. Abanades, Kinetics of the $CaO/Ca(OH)_2$ hydration/dehydration reaction for thermochemical energy storage applications, Ind. Eng. Chem. Res. 53 (2014) 12594-12601.

[36] T. Li, A. Mahecha-Botero, J.R. Grace, Computational fluid dynamic investigation of change of volumetric flow in fluidized-bed reactors, Ind. Eng. Chem. Res. 49 (2010) 6780-6789.

[37] J.F. Davidson, D.P. Harrison, Fluidized Particles, Cambridge University Press, New York, 1963.

[38] I. Barin, Thermochemical data of pure substances, VCH Verlagsgesellschaft Weinheim, Germany, 1989.

Table 1. Summary of the most relevant testing operation conditions and results corresponding to hydration

Hydration										
Test nº	M_{CaO} (kg)	$T_{Bed,in}$ (ºC)	$T_{Bed,max}$ (ºC)	$v_{H2O,input}$	$v_{H2O,eq}$ TBed in *	$v_{H2O,eq}$ TBed max *	$u_{Tbed, in}$ (m/s)	X_{max} (mol H_2O/mol Ca total)	N_{Ca} active (mol)	t_{exp} (min)
1	2.5	460	510	0.84	0.30	0.81	0.39	0.45	20.1	50
2	2.1	450	487	0.57	0.24	0.52	0.39	0.20	7.5	58
3	2.1	494	506	0.82	0.60	0.76	0.39	0.26	9.8	65
4	2.1	395	485	0.57	0.06	0.50	0.39	0.51	19.1	41
5	1.8	451	495	0.84	0.24	0.61	0.39	0.28	9.0	22
6	1.8	390	481	0.57	0.06	0.46	0.43	0.35	11.3	23
7	2.5	395	489	0.57	0.06	0.54	0.43	0.11	4.9	18
8	1.8	440	485	0.57	0.19	0.50	0.46	0.15	4.8	18
9	2.5	455	490	0.67	0.27	0.55	0.39	0.09	4.0	18
10	2.1	450	508	0.82	0.24	0.78	0.35	0.10	3.8	28

* Equilibrium $H_2O_{(v)}$ partial pressures provided by Barin [38]

Table 2. Summary of the most relevant testing operation conditions and results

corresponding to dehydration

						Dehydration				
Test nº	M_{CaO} (kg)	$T_{Bed,in}$ (ºC)	$T_{Bed,min}$ (ºC)	$\nu_{H2O,input}$	$\nu_{H2O,eq}$ TBed in *	$\nu_{H2O,eq}$ TBed min *	$u_{Tbed,\,in}$ (m/s)	X_{max} (mol H_2O/mol Ca total)	$N_{Ca\,active}$ (mol)	t_{exp} (min)
11	2.1	450	450	0.08	0.24	0.24	0.50	0.35	13.1	180
12	2.2	500	470	0.08	0.67	0.37	0.53	0.39	15.3	23
13	2.1	500	500	0.08	0.67	0.67	0.53	0.35	13.1	13
14	1.8	500	450	0	0.67	0.24	0.50	0.28	9.0	22
15	2.5	500	480	0	0.67	0.45	0.50	0.30	13.4	14
16	2.5	455	431	0	0.27	0.15	0.31	0.34	15.2	63
17	1.8	450	441	0	0.24	0.19	0.40	0.30	9.6	33
18	1.8	460	431	0	0.30	0.15	0.47	0.22	7.1	22
19	2.5	460	433	0	0.30	0.16	0.47	0.18	8.0	30
20	2.1	450	446	0	0.24	0.22	0.46	0.27	10.1	43

* Equilibrium $H_2O_{(v)}$ partial pressures provided by Barin [38]
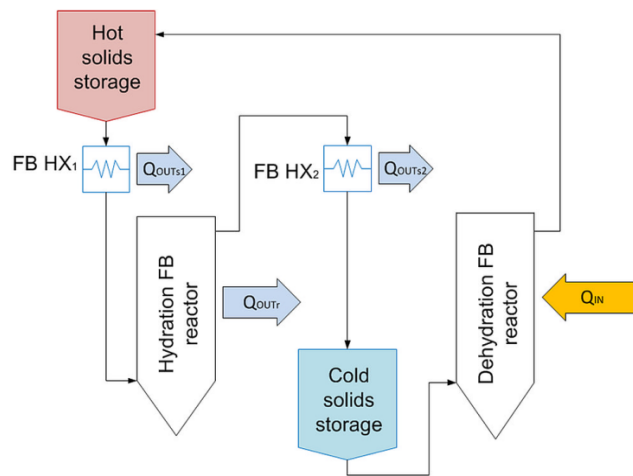
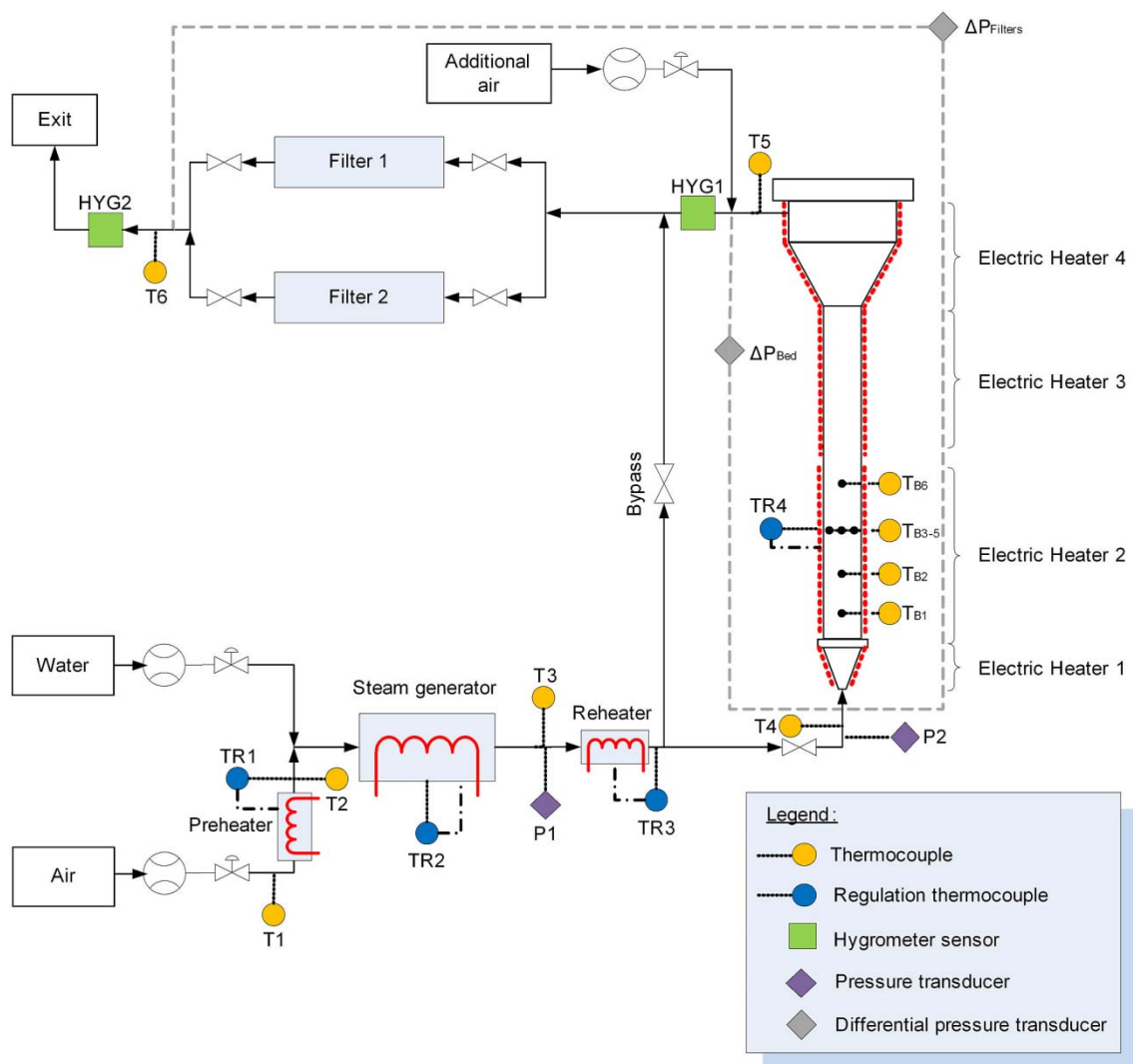**Figure 1.** Basic schematic process view of the CaO/Ca(OH)$_2$ energy storage system.

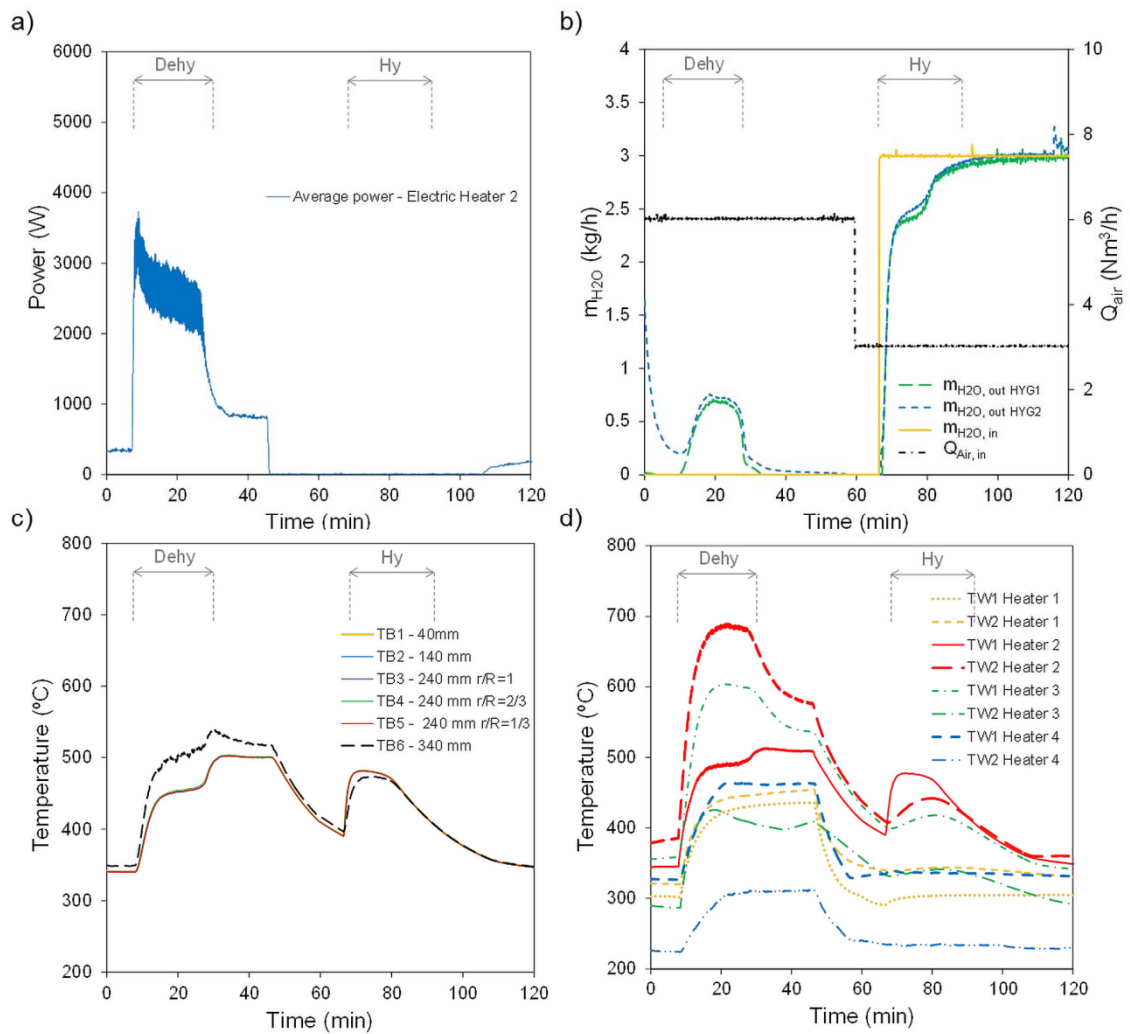**Figure 2.** Schematic view of the experimental setup.

Figure 3. Main signals measured vs time during a typical dehydration/hydration test in the batch fluidized bed using 1.8 kg of CaO/Ca(OH)$_2$ solids (dp=200-400 μm). **a)** Power delivered to the reaction section by the Electric Heater 2. **b)** Input and output mass flows of H$_2$O$_{(v)}$ (m$_{H2O}$) and volumetric flow of air (Q$_{Air}$). **c)** Temperatures of the bed of solids and **d)** at the electric heater walls.
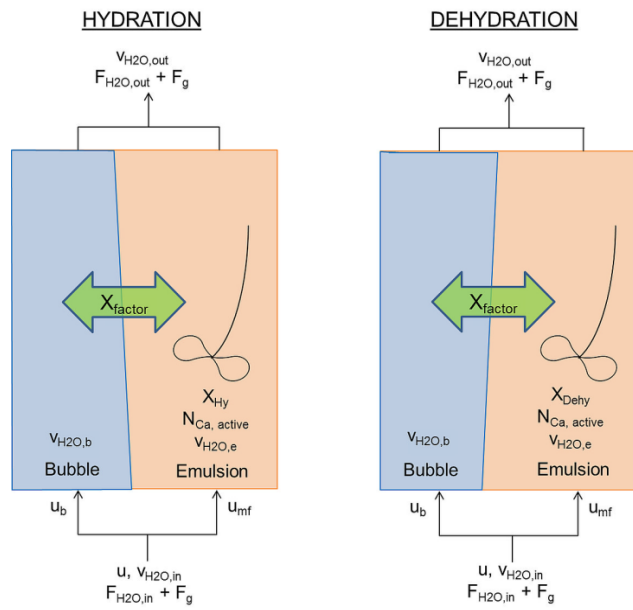
Figure 4. Schematic representation of the reactor during hydration (left) and dehydration (right), with an introduction to the notation employed for the main variables in the reactor model.
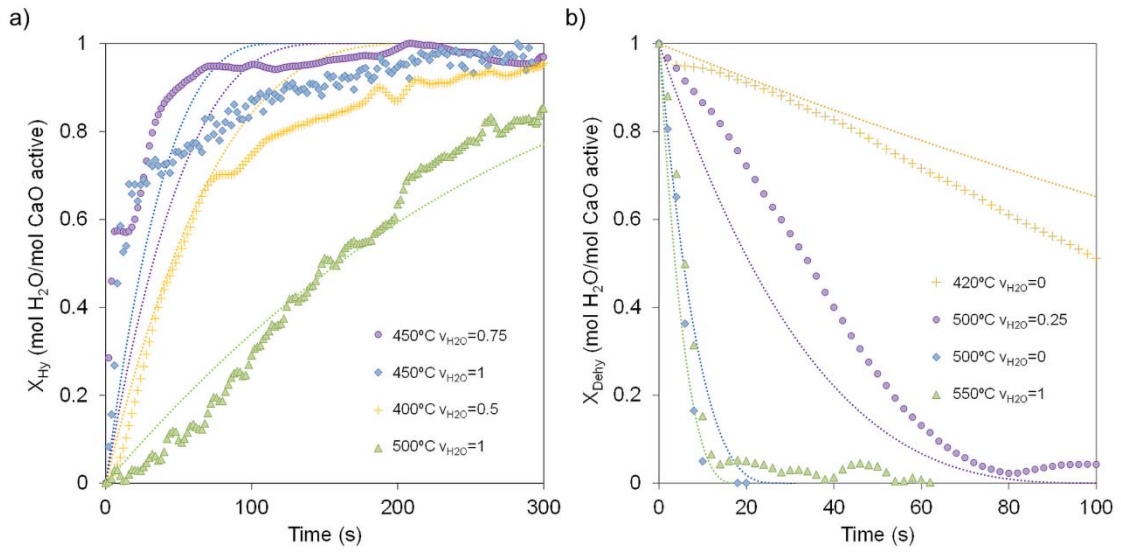
Figure 5. a) Hydration and **b)** dehydration conversion of the active CaO (X_{Hy} and

X_{Dehy}) vs time for the CaO sample provided by Carmeuse for a dp of 100-200 µm tested

at different temperatures and $H_2O_{(v)}$ partial pressures. Lines corresponding to the kinetic

model [35] applying $k_{Hy}=0.2 \times k_{Hy\ ref}$ and $k_{Dehy}=k_{Dehy\ ref}$. Note the different time scale in
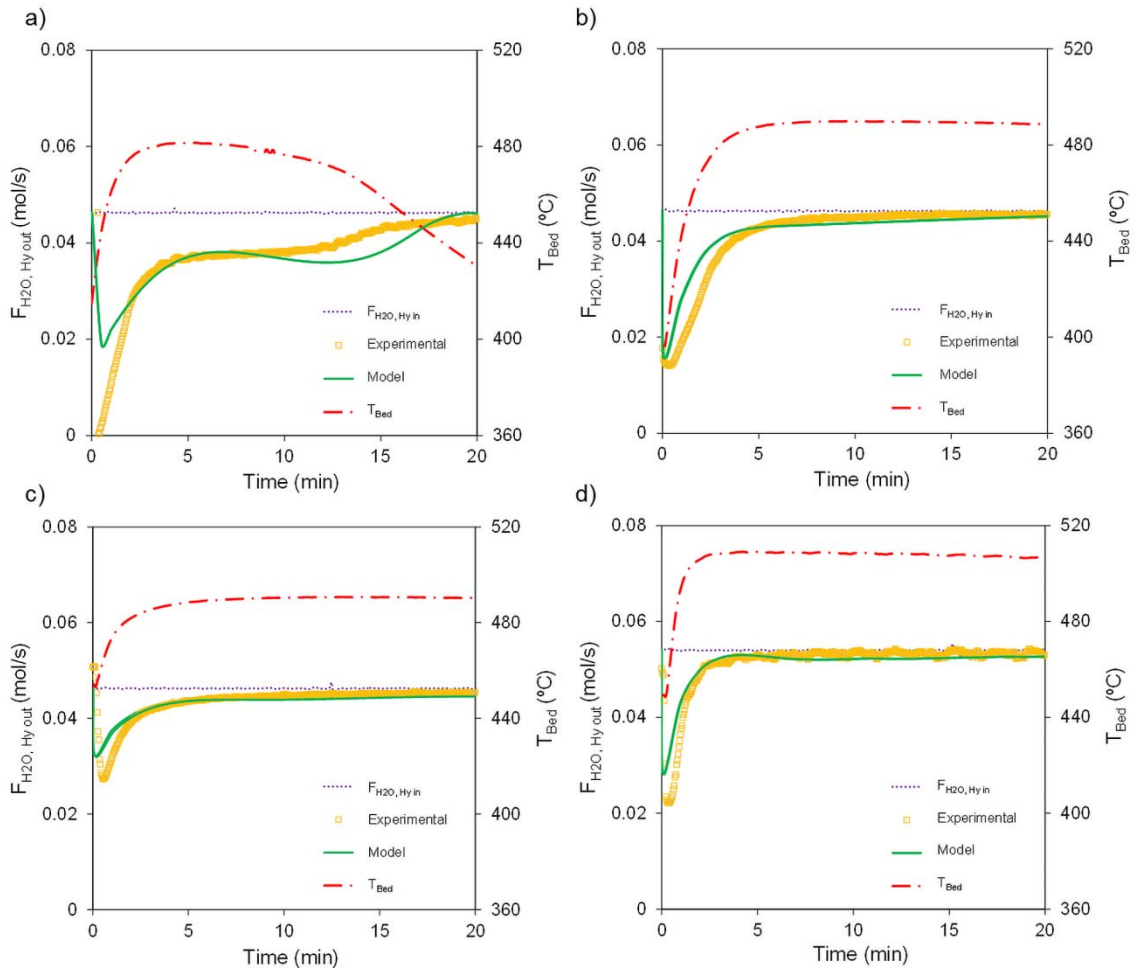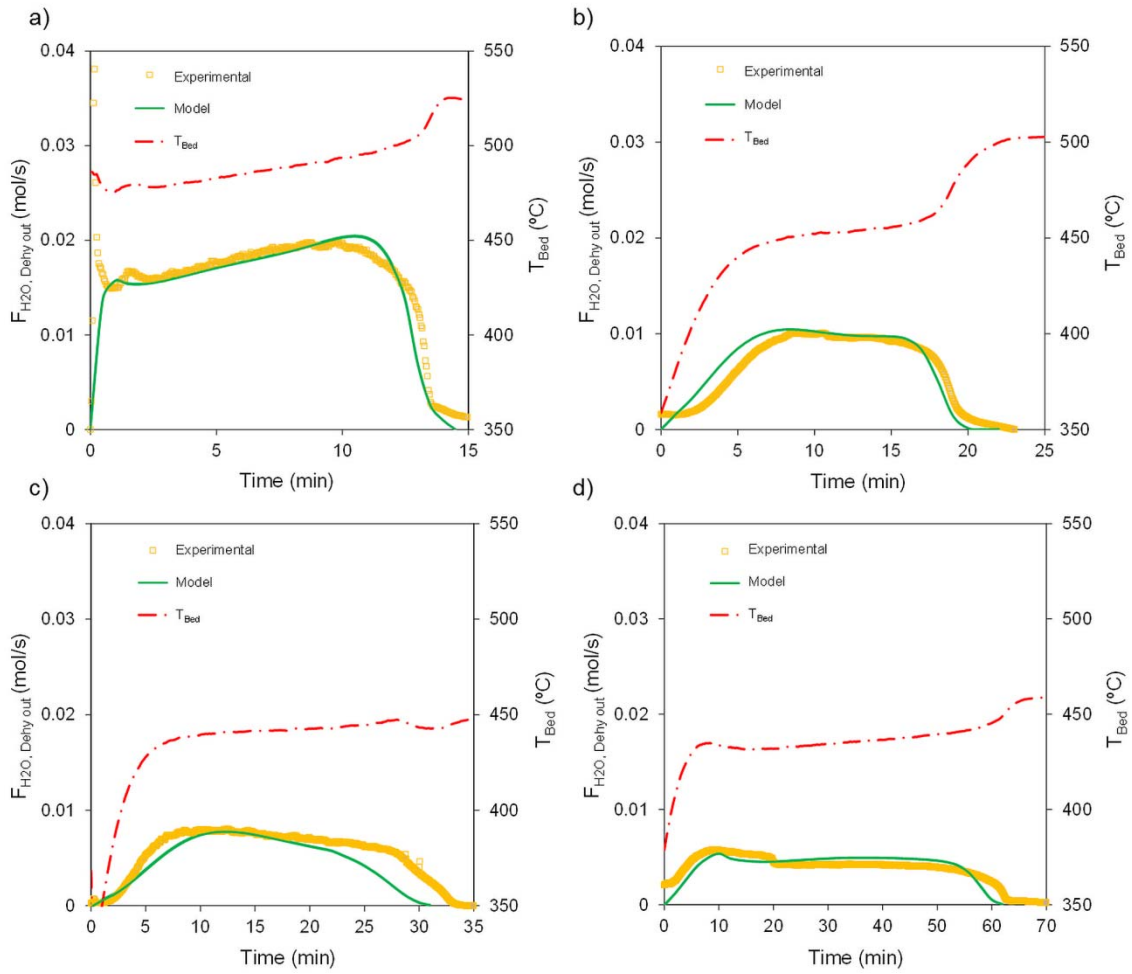
both graphs.

Figure 6. Experimental and model-predicted molar flow of $H_2O_{(v)}$ during hydration ($F_{H2O, Hy\ out}$) and bed temperature (T_{Bed}) vs time for tests **a)** nº 6, **b)** nº 7, **c)** nº 8 and **d)** nº 9. In all cases the $X_{factor}=1.5$. The input molar flow of $H_2O_{(v)}$ ($F_{H2O,in}$) is represented as dotted lines for reference.

Figure 7. Experimental and model-predicted molar flow of $H_2O_{(v)}$ during dehydration ($F_{H2O, Dehy out}$) and bed temperature (T_{Bed}) vs time for tests **a)** nº 15, **b)** nº 14, **c)** nº 17 and **d)** nº 16. In all cases the $X_{factor}=1.5$.
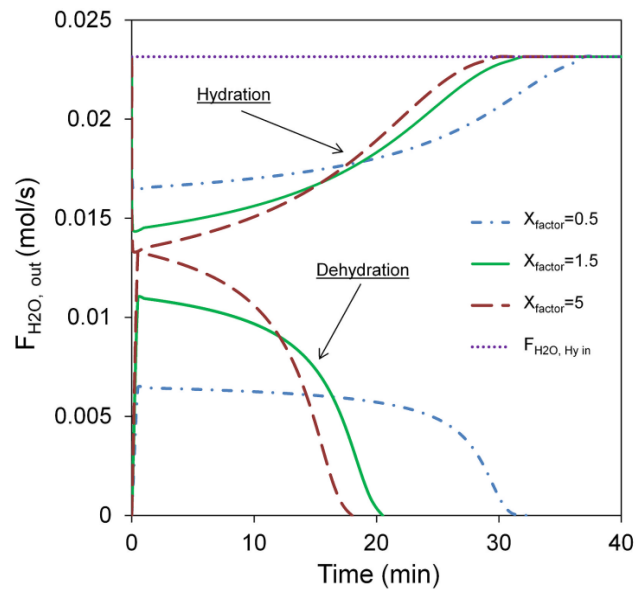
Figure 8. Effect of the X_{factor} on the prediction given by the reactor model. T_{Bed}=455ºC, $N_{Ca\ active}$=10 mol, $v_{H2O,\ Hy}$=0.5, $v_{H2O,\ Dehy}$=0, $u_{Tbed,\ Hy}$=0.3 m/s and $u_{Tbed,\ Dehy}$=0.5 m/s.